SCIENTIFIC REPORTS

OPEN

# Rotatable precipitates change the scale-free to scale dependent statistics in compressed Ti nano-pillars

Received: 30 July 2018
Accepted: 14 February 2019
Published online: 07 March 2019

Yan Pan[1], Haijun Wu[2], Xiaofei Wang[1], Qiaoyan Sun[1], Lin Xiao[1], Xiangdong Ding[1], Jun Sun[1] & Ekhard K. H. Salje[1,3]

**Compressed nano-pillars crackle from moving dislocations, which reduces plastic stability. Crackling noise is characterized by stress drops or strain bursts, which scale over a large region of sizes leading to power law statistics. Here we report that this "classic" behaviour is not valid in Ti-based nanopillars for a counterintuitive reason: we tailor precipitates inside the nano-pillar, which "regulate" the flux of dislocations. It is not because the nano-pillars become too small to sustain large dislocation movements, the effect is hence independent of size. Our precipitates act as "rotors": local stress initiates the rotation of inclusions, which reduces the stress amplitudes dramatically. The size distribution of stress drops simultaneously changes from power law to exponential. Rotors act like revolving doors limiting the number of passing dislocations. Hence each collapse becomes weak. We present experimental evidence for Ti-based nano-pillars (diameters between 300 nm and 2 μm) with power law distributions of crackling noise $P(s) \sim s^{-\tau}$ with $\tau \sim 2$ in the defect free or non-rotatable precipitate states. Rotors change the size distribution to $P(s) \sim \exp(-s/s_0)$. Rotors are inclusions of ω-phase that aligns under stress along slip planes and limit dislocation glide to small distances with high nucleation rates. This opens new ways to make nano-pillars more stable.**

Building progressively smaller technological devices requires revaluation of size-independent material engineering[1]. A main problem is brittleness at small scales in metals, alloys, multi-ferroics and other functional materials. Experimental observations first indicated that "smaller is stronger"[2], but then it was found that intermittent stress singularities (jerks) also increase. Such tendency that "smaller is wilder"[3] contrasts Gaussian plastic fluctuations in large samples[3] with scale-free intermittency at micro and nano scales for the same materials[4–10]. The abrupt strain jumps in quasi-statically loaded micro-/nano-components endanger structural stability and the associated unpredictability raises serious challenges for applications[10,11].

Stress serrations of nano-pillars are common[6,7,12–14] when stress drops, energies, and waiting times are power law distributed with universal properties[4,15–21]. The underlying atomic mechanism of serration is often the propagation of dislocations along slip planes inside nano-pillars. To avoid this inhomogeneous plastic slip, various inclusions have been introduced to inhibit dislocation avalanche propagation. In duralumin pillars, the slip steps on the 1 μm pillar are smaller and more homogeneously distributed, compared with the Al counterpart[22], which suggests smaller strain burst behaviour with precipitation hardening in pillars. However, below several micron, intermittent plastic flow is also observed in duralumin micropillars[22] and Ni-based oxide-dispersion strengthened alloys[23]. In addition, there are also experimental observations indicating that strain bursts are promoted by introducing nanoscale $\eta'$ phase to Al micropillars[24], because a number of dislocations are first trapped by precipitates, and then suddenly move in a correlated fashion, leading to large bursts. However, here we report that the number of serrations, their energy distribution and their inter-event times can be tailored in Ti-based nano-pillars by the inclusion of pinning centres that reduce dislocation movements. Our pinning centres are small inclusions

[1]State Key Laboratory for Mechanical Behavior of Materials, Xi'an Jiaotong University, Xi'an, 710049, China. [2]Department of Materials Science and Engineering, National University of Singapore, Singapore, 117575, Singapore. [3]Department of Earth Sciences, University of Cambridge, Cambridge, CB2 3EQ, United Kingdom. Correspondence and requests for materials should be addressed to X.D. (email: dingxd@mail.xjtu.edu.cn) or E.K.H.S. (email: ekhard@esc.cam.ac.uk)

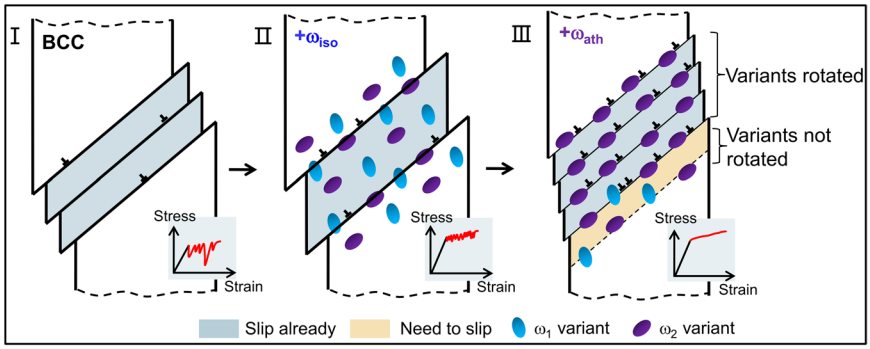


**Figure 1.** Design concept for avalanches and yield strength engineering in β-Ti alloy nano-pillars. The three scenarios are: no ω phase precipitates and large avalanches (I), inclusions of $\omega_{iso}$ precipitates and reduced avalanches (II), and rotor inclusions of $\omega_{ath}$ precipitates with even smaller fluctuations (III).

of ω-phase, which can easily be introduced by appropriate heat treatment and slight changes of the chemical composition. We observed that rotating ω-phase inclusions change crackling noise from power-law serration to exponential distributions of stress drops and waiting times between stress drops. This is of fundamental importance: we know so far of no process that destroys the space and time invariance of stress drops[25–28] in such a simple doping process. Stress drop mechanisms and related processes were discussed in some theoretical papers[27–32] while simple analytical theories always lead to power law singularities[33–35]. We have discovered a material where we can switch between scale invariant behaviour in the power law regime to cut-off dominated processes with well-defined energy and time scales. The wider implication is that we are now able to improve the properties of nano-pillars to make them stronger and more stable[36,37]. We will show that compression in rotor-stabilized nano-pillars does not lead to macroscopic slip band and show smooth strain-stress curves.

## Materials Design

ω inclusions in β-Ti alloys are either a metastable athermal phase, which is produced by rapid quenching, or isothermal phases when samples are aged at appropriate temperatures. Small sized athermal ω ($\omega_{ath}$) precipitates form by local collapse of the {111} planes of the β phase (BCC structure) via a shuffle mechanism with four crystallographic variants[38]. The size range of the precipitates is 2–10 nm. The isothermal ω ($\omega_{iso}$) precipitates grow from aged $\omega_{ath}$ inclusions. The growing $\omega_{iso}$ precipitates coarsen and reject stabilizing elements into the surrounding β matrix[39,40]. Thus, the $\omega_{iso}$ precipitate is a stable phase, while $\omega_{ath}$ precipitate represents a metastable phase with the same composition as the β matrix[39,40]. We make use of the different properties of ω precipitates to influence dislocation movements. Three scenarios were designed to represent different degrees of confinement and dynamics of dislocation movements (Fig. 1). In the first scenario of BCC nano-pillars without precipitates, dislocations can travel freely and stress drops are large. The stress-strain curves (displacement-controlled loading) show large stress fluctuations during deformation[7,41]. In the second scenario, $\omega_{iso}$ precipitates hinder the movement of dislocations and, thus, the amplitudes of stress drops are reduced[14,42]. In the third scenario, $\omega_{ath}$ precipitates further reduce the drop amplitudes and keep high yield strength. These $\omega_{ath}$ precipitates act as rotors and enable nucleation of dislocations so that a very large number of small dislocations with many dense slip lines coexist and the strain-stress curve becomes almost smooth.

Experimentally, nano-pillars of β-Ti alloys (Ti-32Mo, Ti-20Mo and Ti-10V-2Fe-3Al) were manufactured with sizes between 300 nm and 2 μm and bulk compositions: (a) Ti-32Mo without ω phase precipitates, (b) Ti-20Mo with $\omega_{iso}$ precipitates, and (c) Ti-10V-2Fe-3Al with $\omega_{ath}$ precipitates ($\omega_{ath}$-Ti-1023). The detailed heat treatment procedures are described in the section on sample preparation. Microstructures were characterized with transmission electron microscope (TEM) for the three types of β-Ti alloys, as shown in the Supplementary Fig. S1. Both $\omega_{ath}$ and $\omega_{iso}$ precipitates in the present cases have similar mean diameter of 3∼4 nm and similar mean spacing of 6∼8 nm.

## Results

**Comparison of mechanical behavior.** Figure 2 shows the effect of precipitates on compression in three types of nano-pillars (Ti-32Mo, $\omega_{iso}$-Ti-20Mo, and $\omega_{ath}$-Ti-1023 alloy), additional strain-stress curves are shown in Supplementary Fig. S2. The "jerkiness" of the strain-stress curve decreases from (a) to (b) at the large pillar sizes, while the reduction becomes not obvious at small pillar sizes. The "jerkiness" dramatically decreases in (c) at all pillar sizes. It indicates that $\omega_{iso}$ can reduce the stress fluctuations at the large pillar sizes while the $\omega_{ath}$ can reduce the stress fluctuations at all pillar sizes. It is noted that the stress-strain curves of the $\omega_{iso}$-Ti-20Mo alloy (Fig. 2b) show obvious stress oscillation, especially for 1.0 and 2.0 μm pillars, which is caused by the activation of large slip bands[42]. In contrast, the stress-strain curves of $\omega_{ath}$-Ti-1023 alloy (Fig. 2c) exhibit continuous stable plastic flow phenomenon. Thus, we simply calculate the slope of the curve at stress increasing region from 6% to 11% to represent the ω strengthening effect. The calculated slopes in $\omega_{iso}$-Ti-20Mo alloy are 6040 MPa for 2.0 μm pillar and 5308 MPa for 1.0 μm pillar, while the slopes in $\omega_{ath}$-Ti-1023 alloy are 3660 MPa for 2.0 μm pillar and 3886 MPa for1.0 μm pillars. The result shows that $\omega_{iso}$ precipitate exhibit a higher strengthening effect and a less stable effect on plasticity than the $\omega_{ath}$ precipitate. After deformation, multiple large slip bands were found after

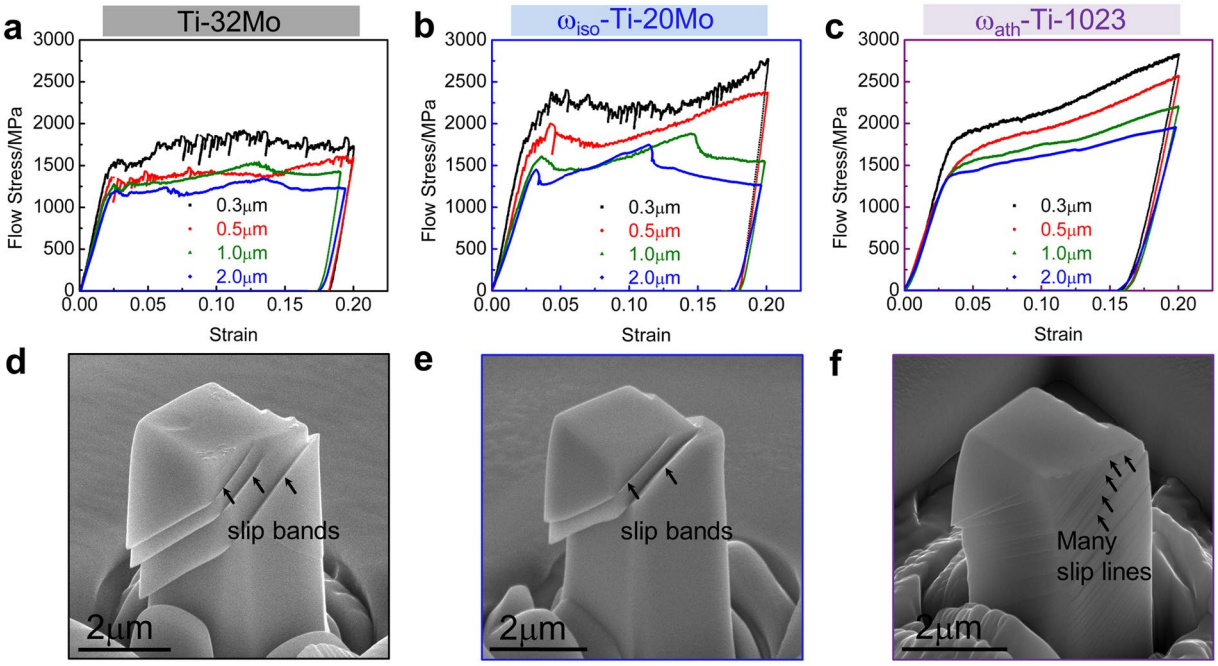


**Figure 2.** Compression test on β-Ti alloy nano-pillars. (**a**–**c**) Comparison of mechanical behavior for the three scenarios in Fig. 1 and different pillar sizes. (**d**–**f**) The SEM images show the equivalent slip configurations for the three alloys of 2 μm pillars.

deformation in (a), (b), and many slip lines (but no slip bands) with small amplitudes occur on the pillar surface in (c). Only one slip system is activated when the samples are deformed in <011>. The slip planes have angles of ca.52° with the {011} top surface and represents the {112} <111> slip system.

**Statistics for stress drops and waiting times.** The stress-strain curves in Fig. 2 were analysed by calculating the squared temporal derivatives of the stress: $(d\sigma/dt)^2$ [30,31,43]. The detailed calculations are described in the section of statistics method and Supplementary Fig. S3. The avalanche statistics are shown for the three cases in Fig. 3a–c containing some very large events, which correspond to spanning slips, and a multitude of smaller events of dislocation glide. Only the latter are included in the probability distribution function (PDF) because the sizes of the largest stress drops are determined by boundary conditions (spanning avalanches from surface to surface). The PDFs are strongly size dependent and collapse onto a master curve when the amplitudes are normalized by the average amplitude for each system.

Power law distributions were found only for the first two scenarios. The fitted power law exponents are almost identical: 1.96 and 2.05 with the incorporation of $\omega_{iso}$ precipitates. A drastic change of the PDF occurs in the third scenario when $\omega_{ath}$ precipitates are introduced. Crackling noise of stress drops (measured as normalized $(d\sigma/dt)^2$) now follows a distribution $P(s) = s^{-\tau}\exp(-s/s_1)(1-\exp(-s/s_2))$ [44] with $\tau = 1.3$, $s_1 = 2.68$ and $s_2 = 15.64$ where the high energy cut-off $s_1$ dominates. Waiting time analysis shows the same sequence (Fig. 3d–f): the first two scenarios show power law distributed waiting times (normalized waiting time: waiting time/<waiting time>) with exponents 1.95 and 1.92. The third scenario yields an exponential distribution $P(s) = 0.29 * \exp(-s/s_o)$ with $s_o$ normalized by the average waiting time. In the Supplementary Fig. S4, we show how the exponents are estimated by Maximum Likelihood method [44,45] for stress drops and waiting times.

**Deformation characterization.** The deformation mechanisms of the three β-Ti alloy pillars are analysed by (scanning) transmission electron microscopy ((S)TEM). We observe that deformation of Ti-32Mo pillar is mediated by dislocation slip (Supplementary Fig. S5), which is typical for BCC alloys, and shows large avalanche amplitudes in stress-strain curves [7,41]. Precipitates hinder such dislocation movements in the slip plane of $\omega_{iso}$-Ti-20Mo pillars (Supplementary Fig. S6). Further loading increases the stress concentration in front of $\omega_{iso}$ precipitate, and leads to dislocations cut through the precipitate [42,46]. The movement of dislocations is reduced and avalanche amplitudes are smaller than in the first scenario.

Rotations of $\omega_{ath}$ precipitates occur in $\omega_{ath}$-Ti-1023 pillars under applied stress. TEM images of a $\omega_{ath}$-Ti-1023 pillar with 5% compressive strain show many parallel slip planes (Fig. 4a). Figure 4a is the enlarged view of the purple square area of the lower-right inset. It is clearly seen that the slip region in Fig. 4a stems from the deformed area. Selected area electron diffraction (SAED) of the non-slip region (blue rectangle in Fig. 4a) show that the diffraction intensities of two equivalent $\omega_{ath}$ variants ($\omega_{ath1}$ and $\omega_{ath2}$) are almost identical. Dark-field TEM images using $\omega_{ath1}$ and $\omega_{ath2}$ reflections (Fig. 4b,c) further prove that the concentrations of $\omega_{ath1}$ and $\omega_{ath2}$ precipitates in the non-slip region are identical. The SAED patterns of the slip region show only a weak diffraction intensity of $\omega_{ath1}$, and a strong diffraction intensity of $\omega_{ath2}$ (red rectangle in Fig. 4a). The related dark-field TEM images

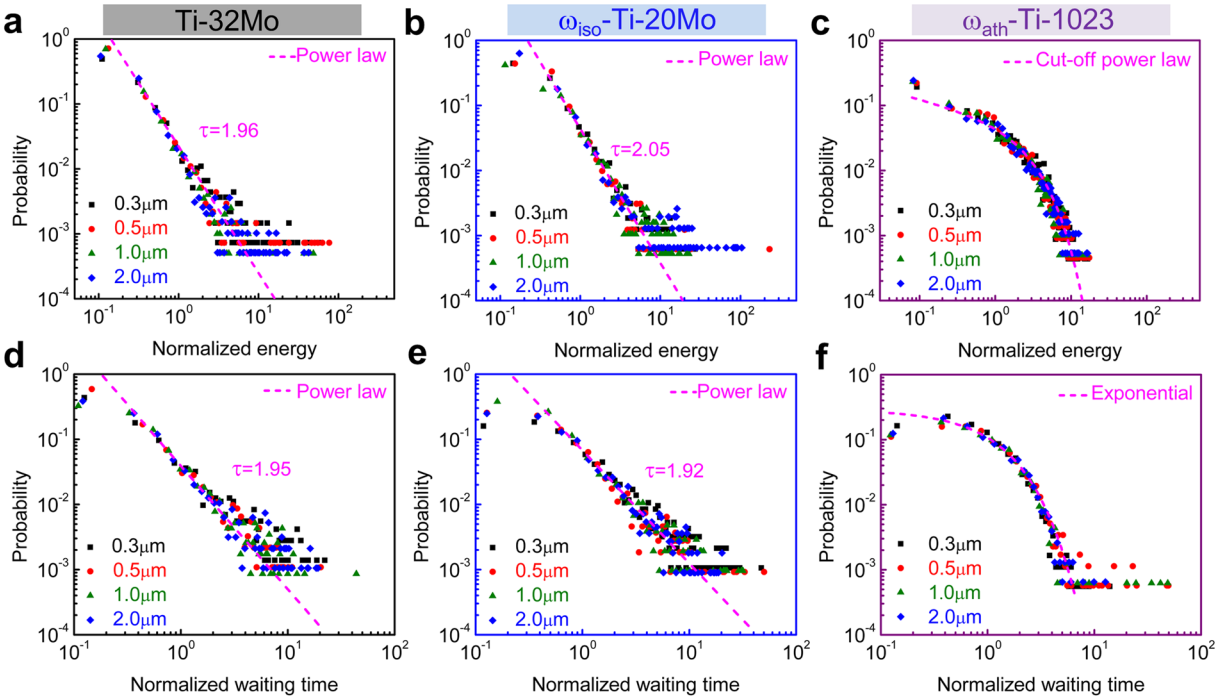


**Figure 3.** Probability distribution functions for stress drops and waiting times for the three scenarios in Fig. 2. (**a**–**c**) The stress drops are normalized by the average stress drop, which rescales all curves to be independent of the pillar diameter. The fitting line in (**c**) is cut-off power law $P(s) = s^{-1.3}\exp(-s/2.68) * (1 - \exp(-s/15.64))$. (**d**–**f**) The waiting times are normalized by the average waiting time, which rescales all curves to be independent of the pillar diameter. The fitting line in (**f**) is exponential distribution with $P(s) = 0.29 * \exp(-s/s_o)$, where $s_o$ is normalized to 1.0.

using $\omega_{ath1}$ and $\omega_{ath2}$ reflections (Fig. 4d,e) show that $\omega_{ath1}$ precipitates almost disappeared, while the number of $\omega_{ath2}$ approximately doubled. The absence of the $\omega_{ath1}$ inside slip planes indicates a transformation from $\omega_{ath1}$ to $\omega_{ath2}$ under stress. STEM annular bright-field (ABF) lattice images of the slip region (Fig. 4f) also show that $\omega_{ath1}$ variant rotate to $\omega_{ath2}$ variant. The $\omega_{ath}$ phase is identified by the atomic structural feature, which is used in reference[40]. Typical $\omega_{ath2}$ crystal lattices are highlighted by six blue dots. There is no sharp boundary between β matrix and $\omega_{ath}$ phase as the structural similarity and coherent nature of the interface. The blue ellipses in Fig. 4f are approximate indications of the $\omega_{ath2}$ phase boundaries. Along the slip direction, $\omega_{ath2}$ is preferred, while $\omega_{ath1}$ is not preferred from Fig. 4d,e. However, we do find that some $\omega_{ath1}$ structures (represented by six green spots) still exist in the $\omega_{ath2}$ phase region. As the average $\omega_{ath}$ lattice parameter is 3.27 nm, the fact that $\omega_{ath2}$ and $\omega_{ath1}$ phase co-exist within 2 nm-region along the slip bands indicates some $\omega_{ath1}$ phase is not rotated and retains its previous orientation. The Burger's vector orientation of most dislocations around $\omega_{ath}$ precipitate are consistent with the slip direction (shown in Fig. 4f,g), while the orientation of dislocation (numbered 2) in front of $\omega_{ath}$ precipitate derivate from the slip direction, where the dislocation is obstructed by the $\omega_{ath}$ precipitate along its pathway. The accumulation of dislocations in front of $\omega_{ath}$ precipitate will lead to an obvious lattice distortion and thus its Burger's vector orientation is different from other dislocations. Therefore, the variant rotation is activated by stress concentration of dislocation pile-ups in front of $\omega_{ath}$ inclusions, and then facilitates the nucleation of new dislocations (indicated by blue dotted boxes in Fig. 4f). The propagation of dislocations is now blocked and restarts on the other side of the rotated $\omega_{ath}$ variant (or other sites where the stress concentration is high) with further loading, leading to many tiny slip lines, but no big slip bands.

To further verify the existence of dislocations around $\omega_{ath}$ precipitate, the ABF lattice image (Fig. 4f) was analyzed by Geometric Phase Analysis (GPA)[47,48]. GPA technique is described in the Supplementary Note 1. Figure 4g shows the GPA results choosing $(110)_\beta$ and $(112)_\beta$ to calculate strain. The butterfly-like strain field in the selected region (with blue dotted line in Fig. 4g) reveals the positions of dislocation core. The related insert inverse fast Fourier transform images further confirm these strain regions are close to dislocations.

## Discussion

**The precipitate effect on plasticity stability.** In this work, the jerk energy is defined as the square of stress drop rate, $(d\sigma/dt)^2$. Figure 5a shows that the average jerk energy decrease from Ti-32Mo to $\omega_{iso}$-Ti-20Mo at the large pillar size, while the reduction of jerk energy becomes uncertain at small pillar sizes. However, $\omega_{ath}$ reduces the jerk energies and improves the plasticity stability in $\omega_{ath}$-Ti-1023 at all pillar sizes. The reason is that the $\omega_{ath}$ precipitates act as pinning and nucleation centers in the slip region as described above. The rotation of $\omega_{ath}$ precipitates strongly pins and blocks the avalanche movement of dislocations. Dislocations can now only glide over small distances. The rotation of $\omega_{ath}$ precipitates also leads to dislocation nucleation with high rates.

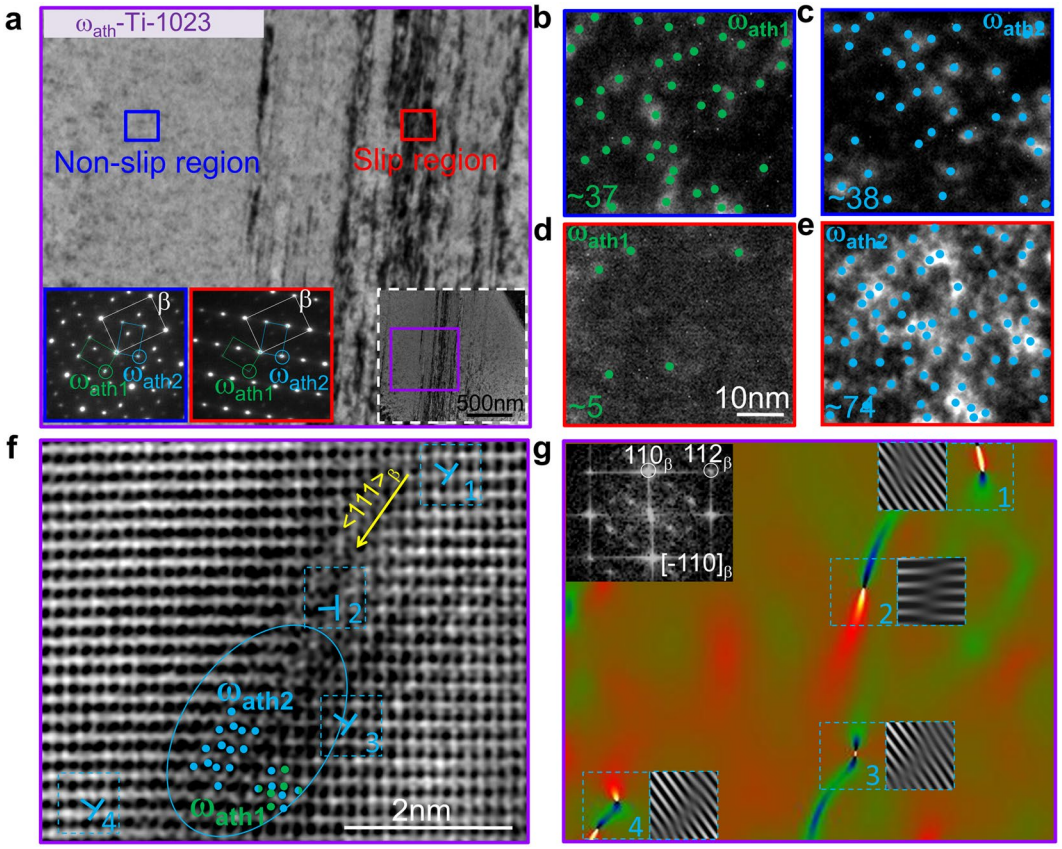


**Figure 4.** Deformation features of $\omega_{ath}$-Ti-1023 pillars with 5% compression strain. (**a**) Bright-field image of deformed pillar with many slip lines, which is the enlarged view of the purple square area of the lower-right inset containing the whole slip region. The blue and red rectangles display typical non-slip and slip regions. The lower-left insets correspond to selected area electron diffraction (SAED) patterns along the $<011>_{\beta}$ zone axis showing two $\omega_{ath}$ variants reflections. The $\omega_{ath1}$ and $\omega_{ath2}$ are two crystallographic variants of the $\omega_{ath}$ phase. (**b**,**c**) Dark-field images using the $\omega_{ath1}$ and $\omega_{ath2}$ reflections corresponding to the blue rectangle, which shows that the number of $\omega_{ath1}$ and $\omega_{ath2}$ precipitates is almost the same (~38) in non-slip region. These white speckles are the $\omega_{ath}$ precipitates. White $\omega_{ath1}$ and $\omega_{ath2}$ precipitates are highlighted by green and blue dots, respectively. (**d**,**e**) Dark-field images corresponding to the red rectangle, which shows that in slip region the number of $\omega_{ath1}$ precipitates is near to zero and the number of $\omega_{ath2}$ (~74) is increased as double as the non-slip region. (**f**) STEM annular bright-field (ABF) lattice image shows dislocations pile-up in front of $\omega_{ath}$. They induce $\omega_{ath}$ variant rotation and produce new dislocations on the rear of the rotated $\omega_{ath}$ variant. Typical $\omega_{ath1}$ and $\omega_{ath2}$ crystal lattices are highlighted by six green and blue dots, respectively. The yellow arrow shows the slip direction. (**g**) Detailed characterization of the dislocations around $\omega_{ath}$ precipitate in (**f**) by Geometric phase analysis (GPA) choosing $(110)_{\beta}$ and $(112)_{\beta}$ to calculate strain. Strain regions are highlighted by rectangles. The inset in the top left shows the fast Fourier transform (FFT) results of (**f**). The inset of two inverse FFT images with $(110)_{\beta}$ and $(112)_{\beta}$ reflections confirm that the highlighted strain regions by GPA are regions with dislocation.

Supplementary Fig. S7 shows dense slip traces occurs in $\omega_{ath}$-Ti-1023 pillar in comparison with Ti-32Mo and $\omega_{iso}$-Ti-20Mo pillars, which indicates large conservation of dislocations in $\omega_{ath}$-Ti-1023.

The rotation of $\omega_{ath}$ precipitates is changed in Ti-1023 sample to non-rotatable $\omega_{iso}$ precipitates (called $\omega_{iso}$-Ti-1023) through heat treatment (aging at 250 °C for 1 hour)[49,50]. The $\omega_{iso}$ precipitates have the similar mean diameter of 3.5 nm and mean spacing of 6.75 nm with $\omega_{ath}$ precipitates in Ti-1023 as show in Supplementary Fig. S8. Supplementary Fig. S9 shows obvious stress drops with the probability distribution function of both stress drop and waiting time in $\omega_{iso}$-Ti-1023 pillars now following the power law distribution (see Supplementary Fig. S10): $P(s) \sim s^{-\tau}$ with $\tau \sim 2$ as in $\omega_{iso}$-Ti-20Mo pillars. Thus, the various mechanical behavior of the micropillars mainly depends on the states of the ω precipitates.

**The size effect of the yield stress.** The size effects of yield stress $\sigma_{0.2}$ (stress at 0.2% plastic strain) for three β Ti-alloy pillars are shown in Fig. 5b. We find that "smaller is stronger" is still valid in all the three cases. The $\sigma_{0.2}$ follows a power-law dependence of pillar width D, $\sigma_{0.2} \sim D^m$, and the best fitted m values are close for all the three cases. The size effect is weaker in $\omega_{ath}$-Ti-1023 alloy due to the revolving mechanism of precipitates which facilitate more nucleation of mobile dislocations. Size-dependent strength of precipitated alloys has been investigated in duralumin micropillars[51]. It was found that the mean spacing of the precipitates, as an internal length scale, governs the mean free path of mobile dislocations in the micropillar during deformation, and then

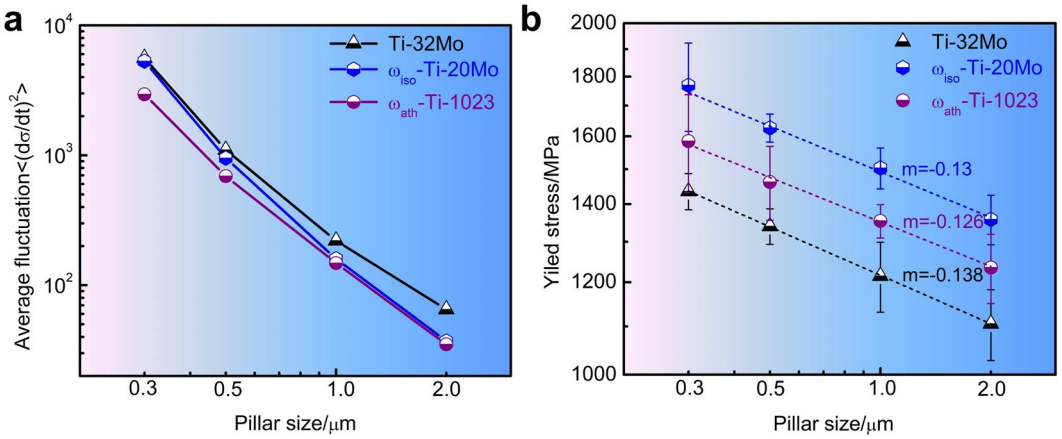


**Figure 5.** Comparison of average fluctuation with sample size (**a**) and size-dependent yield stress at 0.2% plastic strain for three β Ti-alloy pillars (**b**).

determines the strength. The interplay between precipitate strength and dislocation starvation also gives rise to a "weakest size" phenomenon. In the present case, both ω precipitate size and mean spacing are nanoscale in Ti-alloys (Supplementary Fig. S1), however. It takes a large number of precipitates to enhance the pillar strength even in small pillars. All yield stresses $\sigma_{0.2}$ of pillars are larger than the yield stress of $\omega_{iso}$-Ti-20Mo bulk (Fig. S11, 966 MPa). This indicates that there is no "weakest size" for the three cases.

**The effect of deformation on the fluctuation statistics.** Our experiments show that the deformation behavior is strongly correlated with the jerk statistics. For Ti-32Mo alloy without visible precipitates, dislocations can move freely after nucleation and travel to the free surface easily, forming slip bands. During the motion, dislocations can also trigger other dislocations to slip near the original slip plane[21], which makes the plastic deformation to be mainly concentrated on a few of slip bands as seen in Fig. 2d. Thus, these correlated dislocation motions are self-organized with broad power-law-distributed statistics[3], which is scale-free. For $\omega_{iso}$-Ti-20Mo, the precipitates can block the movements of dislocations. Further loading will lead to dislocations cut through the $\omega_{iso}$ precipitates, and dislocations also travel to the free surface, forming slip bands. Finally, dislocation motions share the same characteristics with Ti-32Mo. Therefore, the first two scenarios show little difference, including the statistics and the deformation morphology. But for $\omega_{ath}$-Ti-1023 pillar, there is no slip localization, and the slip lines are on average uniformly distributed throughout the sample. The dislocation motions are blocked by $\omega_{ath}$ precipitates and randomly restarts on the other side of the rotated $\omega_{ath}$ variant or other sites where the stress concentration is high with further loading. Plastic flow then proceeds mainly through small and uncorrelated dislocation motion, confined inside the transient $\omega_{ath}$ variants, which give rise to small and uncorrelated stress fluctuations that is scale dependent. Eventually, the statistics changes from power-law to exponential when $\omega_{ath}$ precipitates are contained in the pillar.

## Conclusion

In summary, we report that highly anisotropic $\omega_{ath}$ phase inclusions, under appropriate conditions, rotate - similar to a revolving door - influencing the progression of dislocations and hence the formation of avalanches. The surprising result of our investigations is the magnitude of the effect: rotors greatly reduce crackling noise and, even more perplexing, change their statistical fingerprint from power laws to exponentials.

## Methods

**Sample preparation.** The virgin Ti-10V-2Fe-3Al alloy sample was solution-treated at 830 °C for 24 hours in vacuum, followed by water quenching to room temperature. The microstructure is a coarse β phase and a high density of athermal ω precipitates (designated as $\omega_{ath}$-Ti-1023). The virgin Ti-20Mo alloy sample was first solution-treated at 1000 °C for 1 hour and quenched in water. The sample was then aged at 350 °C for 1 hour in vacuum, followed by air cooling. The microstructure is a β phase with isothermal ω precipitates (designated as $\omega_{iso}$-Ti-20Mo). The specimen of Ti-32Mo alloy was homogenized at 900 °C for 0.5 hour in vacuum, and followed by air cooling. The corresponding microstructure shows β phase without visible precipitates. Details of the above microstructures are shown in the Supplementary Fig. S1.

The crystallographic orientations of Ti-32Mo, $\omega_{iso}$-Ti-20Mo and $\omega_{ath}$-Ti-1023 alloy specimens were measured using Oxford NordlysNano electron backscatter diffraction (EBSD) detector. Single-crystal pillars with a square cross-section were then fabricated from the [011]-oriented grains in bulk specimens, using a dual Focus Ion Beam(FIB) milling and scanning electron microscope (SEM) in a FEI Dual Beam Helios NanoLab 600 instrument. The width of pillars ranges from 300 nm to 2 μm with an aspect ratio of ~2.5.

**Testing and characterization.** Quantitative compression test was carried out in a Hysitron Ti-950 with a 10 μm flat-tip diamond punch in displacement-controlled mode at a constant nominal strain rate of $5 \times 10^{-4}$/s. In order to ensure the reliability of data, the thermal drift usually was controlled to below 0.05 nm/s in the

compression tests. The cross-sectional area at top surface of the pillar and the initial height were used to calculate engineering stresses and strains. The TEM lamellas of micro-pillar were prepared using the FIB lift-out technique for microstructural observation. The orientation of lamellas remains similar for all samples. Microstructural observations were performed with a JEOL-2100F high-resolution TEM and a FEI TF30 aberration-corrected STEM.

**Statistic methods.** Stress time series are shown in Supplementary Fig. S3a for a 0.3 μm Ti-32Mo micro-pillar. Jerk signals were identified by numerically differentiating the flow stress time series $\sigma(t)$ (Fig. S3b). The average jerk amplitude ($d\sigma/dt$) at the unloading stage was used as a threshold to exclude the background noise of the instrument. The threshold is about 7.72 MPa/s for 300 nm pillar, as shown in the inset of Fig. S3b. The positive peaks of $d\sigma/dt$ curve were filtered out as they correspond to the stress rises in the flow stress time series (Fig. S3c). An avalanche begins when the value of $d\sigma/dt$ curve falls below the threshold ($t_1$ in Fig. S3e) and ends when the derivative increases to above the threshold ($t_2$ in Fig. S3e) and then restarts when the derivative falls below the threshold again ($t_3$ in Fig. S3e). The waiting time is defined as the difference between $t_2$ and $t_3$, that is $t = t_3 - t_2$[14,19]. The jerk amplitude is defined as the height of peak in the squared derivative time series $(d\sigma/dt)^2$ (Fig. S3d,f)[30,31]. The probability to find a certain jerk amplitude (or waiting time) is plotted as a function of amplitude (or waiting time) as Probability Distribution Function (PDF). We applied the Maximum Likelihood (ML) method to determine the power-law exponent[44,52].

## Data Availability

The data that support the findings of this study are available from the corresponding authors upon reasonable request.

## References


1. Zaiser, M. Scale invariance in plastic flow of crystalline solids. *Adv. Phys.* **55**, 185–245 (2006).
2. Uchic, M. D., Dimiduk, D. M., Florando, J. N. & Nix, W. D. Sample dimensions influence strength and crystal plasticity. *Science* **305**, 986–989 (2004).
3. Weiss, J. *et al*. From mild to wild fluctuations in crystal plasticity. *Phys. Rev. Lett.* **114**, 105504 (2015).
4. Friedman, N. *et al*. Statistics of dislocation slip avalanches in nanosized single crystals show tuned critical behavior predicted by a simple mean field model. *Phys. Rev. Lett.* **109**, 095507 (2012).
5. Zaiser, M. Statistical aspects of microplasticity: experiments, discrete dislocation simulations and stochastic continuum models. *J. Mech. Beh. Mater.* **22**, 89–100 (2013).
6. Dimiduk, D. M., Woodward, C., LeSar, R. & Uchic, M. D. Scale-free intermittent flow in crystal plasticity. *Science* **312**, 1188–1190 (2006).
7. Brinckmann, S., Kim, J. Y. & Greer, J. R. Fundamental differences in mechanical behavior between two types of crystals at the nanoscale. *Phys. Rev. Lett.* **100**, 155502 (2008).
8. Ng, K. S. & Ngan, A. H. W. Stochastic nature of plasticity of aluminum micro-pillars. *Acta Mater.* **56**, 1712–1720 (2008).
9. Ng, K. S. & Ngan, A. H. W. Deformation of micron-sized aluminium bi-crystal pillars. *Philos. Mag.* **89**, 3013–3026 (2009).
10. Csikor, F. F., Motz, C., Weygand, D., Zaiser, M. & Zapperi, S. Dislocation avalanches, strain bursts, and the problem of plastic forming at the micrometer scale. *Science* **318**, 251–254 (2007).
11. Argon, A. S. Strain avalanches in plasticity. *Philos. Mag.* **93**, 3795–3808 (2013).
12. Papanikolaou, S., Song, H. & Van der Giessen, E. Obstacles and sources in dislocation dynamics: Strengthening and statistics of abrupt plastic events in nanopillar compression. *J. Mech. Phys. Solids* **102**, 17–29 (2017).
13. Crosby, T., Po, G., Erel, C. & Ghoniem, N. The origin of strain avalanches in sub-micron plasticity of fcc metals. *Acta Mater.* **8**, 123–132 (2015).
14. Zhang, P. *et al*. Taming intermittent plasticity at small scales. *Acta Mater.* **12**, 351–364 (2017).
15. Salje, E. K. H. & Dahmen, K. A. Crackling noise in disordered materials. *Annu. Rev. Conden. Matter. Phys.* **5**, 233–254 (2014).
16. Sethna, J. P. *et al*. Deformation of crystals: Connections with statistical physics. *Annu. Rev. Mater. Res.* **47**, 217–246 (2017).
17. Maaß, R., Wraith, M., Uh, J. T., Greer, J. R. & Dahmen, K. A. Slip statistics of dislocation avalanches under different loading modes. *Phys. Rev. E* **91**, 042403 (2015).
18. Antonaglia, J. *et al*. Bulk metallic glasses deform via slip avalanches. *Phys. Rev. Lett.* **112**, 155501 (2014).
19. Niiyama, T. & Shimokawa, T. Atomistic mechanisms of intermittent plasticity in metals: Dislocation avalanches and defect cluster pinning. *Phys. Rev. E* **91**, 022401 (2015).
20. Janićević, S., Laurson, L., Måløy, K. J., Santucci, S. & Alava, M. J. Interevent correlations from avalanches hiding below the detection threshold. *Phys. Rev. Lett.* **117**, 230601 (2016).
21. Dahmen, K. A., Ben-Zion, Y. & Uhl, J. T. Micromechanical model for deformation in solids with universal predictions for stress-strain curves and slip avalanches. *Phys. Rev. Lett.* **102**, 175501 (2009).
22. Gu, R. & Ngan, A. H. W. Size effect on the deformation behavior of duralumin micropillars. *Scr. Mater.* **68**, 861–864 (2013).
23. Girault, B., Schneider, A. S., Frick, C. P. & Arzt, E. Strength effects in micropillars of a dispersion strengthened superalloy. *Adv. Eng. Mater.* **12**, 385–388 (2010).
24. Hu, T. *et al*. Stabilized plasticity in ultrahigh strength, submicron al crystals. *Acta Mater.* **94**, 46–58 (2015).
25. Denisov, D. V., Lörincz, K. A., Uhl, J. T., Dahmen, K. A. & Schall, P. Universality of slip avalanches in flowing granular matter. *Nat. Commun.* **7**, 10641 (2016).
26. Weiss, J. & Marsan, D. Three-dimensional mapping of dislocation avalanches: clustering and space/time coupling. *Science* **299**, 89–92 (2003).
27. Krisponeit, J. O. *et al*. Crossover from random three-dimensional avalanches to correlated nano shear bands in metallic glasses. *Nat. Commun.* **5**, 3616 (2014).
28. Laurson, L. *et al*. Evolution of the average avalanche shape with the universality class. *Nat. Commun.* **4**, 2927 (2013).
29. Papanikolaou, S. *et al*. Quasi-periodic events in crystal plasticity and the self-organized avalanche oscillator. *Nature* **490**, 517–521 (2012).
30. Ding, X. *et al*. Dynamically strained ferroelastics: Statistical behavior in elastic and plastic regimes. *Phys. Rev. B* **87**, 094109 (2013).
31. Salje, E. K. H., Ding, X., Zhao, Z., Lookman, T. & Saxena, A. Thermally activated avalanches: Jamming and the progression of needle domains. *Phys. Rev. B* **83**, 104109 (2011).
32. Papanikolaou, S. *et al*. Universality beyond power laws and the average avalanche shape. *Nature Phys.* **7**, 316–320 (2011).
33. Cui, Y., Po, G. & Ghoniem, N. Controlling strain bursts and avalanches at the nano-to micrometer scale. *Phys. Rev. Lett.* **117**, 155502 (2016).

34. Dahmen, K. A., Ben-Zion, Y. & Uhl, J. T. A simple analytic theory for the statistics of avalanches in sheared granular materials. *Nature Phys.* **7**, 554–557 (2011).
35. LeBlanc, M., Angheluta, L., Dahmen, K. A. & Goldenfeld, N. Distribution of maximum velocities in avalanches near the depinning transition. *Phys. Rev. Lett.* **109**, 105702 (2012).
36. Jang, D. & Greer, J. R. Transition from a strong-yet-brittle to a stronger-and-ductile state by size reduction of metallic glasses. *Nature Mater.* **9**, 215–219 (2010).
37. Zhu, T. & Li, J. Ultra-strength materials. *Prog. Mater. Sci.* **55**, 710–757 (2010).
38. Banerjee, D. & Williams, J. C. Perspectives on titanium science and technology. *Acta Mater.* **61**, 844–879 (2013).
39. Devaraj, A. *et al*. Experimental evidence of concurrent compositional and structural instabilities leading to ω precipitation in titanium–molybdenum alloys. *Acta Mater.* **60**, 596–609 (2012).
40. Choudhuri, D. *et al*. Coupled experimental and computational investigation of omega phase evolution in a high misfit titanium-vanadium alloy. *Acta Mater.* **130**, 215–228 (2017).
41. Huang, L. *et al*. A new regime for mechanical annealing and strong sample-size strengthening in body centred cubic molybdenum. *Nat. Commun.* **2**, 547 (2011).
42. Chen, W. *et al*. Strong deformation anisotropies of ω-precipitates and strengthening mechanisms in Ti-10V-2Fe-3Al alloy micropillars: precipitates shearing vs precipitates disordering. *Acta Mater.* **117**, 68–80 (2016).
43. Salje, E. K. H., Saxena, A. & Planes, A. Avalanches in functional materials and geophysics Ch.7 (Springer International Publishing, Switzerland, 2017).
44. Salje, E. K. H., Planes, A. & Vives, E. Analysis of crackling noise using the maximum-likelihood method: Power-law mixing and exponential damping. *Phys. Rev. E* **96**, 042122 (2017).
45. Clauset, A., Shalizi, C. R. & Newman, M. E. J. Power-law distributions in empirical data. *SIAM Rev.* **51**, 661–703 (2009).
46. Banerjee, S. & Naik, U. M. Plastic instability in an omega forming Ti-15% Mo alloy. *Acta Mater.* **44**, 3667–3677 (1996).
47. Hÿtch, M. J., Snoeck, E. & Kilaas, R. Quantitative measurement of displacement and strain fields from HREM micrographs. *Ultramicroscopy* **74**, 131–146 (1998).
48. Xin, J. *et al*. Mg vacancy and dislocation strains as strong phonon scatterers in $Mg_2Si_{1-x}Sb_x$ thermoelectric materials. *Nano Energy* **34**, 428–436 (2017).
49. Duerig, T. W., Terlinde, G. T. & Williams, J. C. Phase transformations and tensile properties of Ti-10V-2Fe-3Al, *Metall. Trans. A* **11**, 1987–1998 (1980).
50. Barriobero-Vila, P. *et al*. Phase transformation kinetics during continuous heating of a β-quenched Ti–10V–2Fe–3Al alloy. *J. Mater. Sci.* **50**, 1412–1426 (2015).
51. Gan, K., Gu, R. & Ngan, A. H. W. The weakest size of precipitated alloys in the micro-regime: The case of duralumin. *J. Mater. Res.* **32**, 2003–2013 (2017).
52. Puchberger, S. *et al*. The noise of many needles: Jerky domain wall propagation in $PbZrO_3$ and $LaAlO_3$. *APL Mater.* **5**, 046102 (2017).


## Acknowledgements

This project was supported by the National Natural Science Foundation of China (51320105014, 51621063, 51471129, 51671158), and the 973 Program of China (2014CB644003). E.K.H.S. is grateful to the Leverhulme trust EM-2016-004 and EPSRC (EP/K009702/1) for support. Y.P. would like to acknowledge the help from Shengwu Guo and Yanhuai Li on TEM, and Wenjuan Kou and Mingda Huang for assistance in fabricating micropillars using FIB. Access to the nanoindentation and FIB equipment in CAMP-Nano is also acknowledged.

## Author Contributions

L.X., Q.S. and X.D. designed and supervised the research project. Y.P. carried out the pillar experiments and deformation mechanism analysis. X.W. conducted statistical analysis under the supervision of X.D. and E.K.H.S.; H.W. performed spherical aberration-corrected STEM experiments. J.S. provided valuable comments and suggestions to the work. Y.P., X.D. and E.K.H.S. wrote the paper. All authors contributed to discussions of the results.

## Additional Information

**Supplementary information** accompanies this paper at https://doi.org/10.1038/s41598-019-40526-5.

**Competing Interests:** The authors declare no competing interests.

**Publisher's note:** Springer Nature remains neutral with regard to jurisdictional claims in published maps and institutional affiliations.